ACSNANO
www.acsnano.org
ARTICLE

Compressible, Dense, Three-Dimensional Holey Graphene Monolithic Architecture

Xiaogang Han,[†,⊥] Zhi Yang,[‡,⊥] Bin Zhao,[†] Shuze Zhu,[‡] Lihui Zhou,[†] Jiaqi Dai,[†] Jae-Woo Kim,[§] Boyang Liu,[†] John W. Connell,[∥] Teng Li,[‡] Bao Yang,[‡] Yi Lin,[*,§] and Liangbing Hu[*,†]

[†]Department of Materials Science and Engineering and [‡]Department of Mechanical Engineering, University of Maryland, College Park, Maryland 20742, United States

[§]National Institute of Aerospace, 100 Exploration Way, Hampton, Virginia 23666, United States

[∥]Advanced Materials and Processing Branch, NASA Langley Research Center, Hampton, Virginia 23681, United States

Supporting Information

ABSTRACT: **By creating holes in 2D nanosheets, tortuosity and porosity can be greatly tunable, which enables a fast manufacturing process (*i.e.*, fast removal of gas and solvent) toward various nanostructures. We demonstrated outstanding compressibility of holey graphene nanosheets, which is impossible for pristine graphene. Holey graphene powder can be easily compressed into dense and strong monoliths with different shapes at room temperature without using any solvents or binders. The remarkable compressibility of holey graphene, which is in sharp contrast with pristine graphene, not only enables the fabrication of robust, dense graphene products that exhibit high density (1.4 g/cm^3), excellent specific mechanical strength [18 MPa/(g/cm^3)], and good electrical (130 S/cm) and thermal (20 W/mK) conductivities, but also provides a binder-free dry process that overcomes the disadvantages of wet processes required for fabrication of three-dimensional graphene products. Fundamentally different from graphite, the holey graphene products are both dense and porous, which can enable possible broader applications such as energy storage and gas separation membranes.**

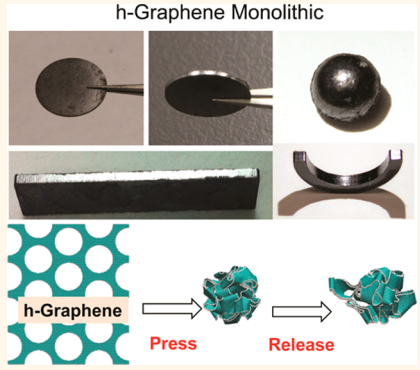

KEYWORDS: *holey graphene, compressible, monolithic devices, binder-free, scalable manufacturing*

From a manufacturing point of view, wet processes have dominated in the fabrication of graphene-based products in advanced applications. These processes include material level manipulation such as solution-based sonication,[1,2] high-shear treatment in liquids,[3] ball milling,[4,5] chemical oxidation−reduction,[6−8] and chemical/electrochemical intercalation for exfoliation of graphite,[9] as well as product form development such as filtration,[10] spinning/slurry coating,[11,12] jet/rod printing,[13−15] spraying,[16−18] freeze-drying,[19,20] electrophoresis,[21] and electrospinning.[22−24] These wet processes have been widely used for the fabrication of graphene films,[25] composites,[26,27] sponges,[28] and aerogels.[29,30] However, the use of large amounts of solvents, very often organic solvents, causes environmental concerns and causes shrinkage and residual stress in the compounds during solvent evaporation.[31] The need for solvent removal by subsequent vacuum filtration or evaporation in order to obtain the final products is both time and energy consuming. Therefore, an alternative process for graphene-based product manufacturing that is energy-saving, highly efficient, and environmentally benign is in urgent demand. However, very few reported methods meet the above requirements. Among a handful of examples, Dai and his colleagues took advantage of dry-milling to mix graphite and active materials for battery electrodes.[32] Another commonly used dry process is cold-pressing. However, it has been a significant challenge to directly press graphene powder into mechanically durable forms.

Topology is critical for properties of 2D materials. Materials can be created by simply changing the topology of 2D materials to impart properties. For example, edges play a critical role in graphene functionalization, as they are often the only sites for attaching/grafting other moieties. The edge length (L) to 2D surface area (A) ratio is $\sim 1/D$ in 2D materials, where D is the lateral dimension of a 2D material. It is often desirable to have a high value of D (large sheet) to enhance, for example, electronic and thermal properties of restacked films. However, a larger D leads to a decrease in edge length per area. Another important characteristic of the edges is their atomic structure, either zigzag or armchair. 2D nanomaterials beyond graphene with two or more types of atoms have more complex chemistry of their edges. For example, zigzag edges for boron nitride (BN) sheets could be either B- or N-terminated, while those for

Received: January 11, 2017
Accepted: March 6, 2017
Published: March 6, 2017

DOI: 10.1021/acsnano.7b00227
ACS Nano XXXX, XXX, XXX−XXX

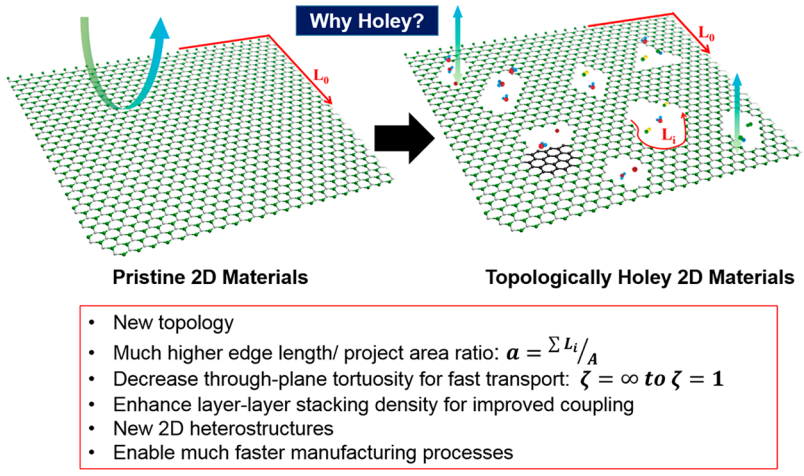

Figure 1. Comparison between pristine 2D materials and their holey counterparts. Topologically different, holey 2D materials can enable structures with potential processing advantages.

MoS_2 sheets could be either Mo- or S-terminated. These different edge structures could have profound effects on their properties and functionalities.[33] As shown in Figure 1, holey 2D materials (H2D) can lead to a range of properties and processes that would be unattainable with the pristine 2D materials (P2D).[34,35] In P2D materials, the area increases by a factor of X^2 when the edge length increases by a factor of X. In H2D, holes result in a modest decrease in area but a drastic increase in edge length, and thus a significantly increased edge-to-area ratio. H2D, with a larger edge-to-area ratio, enable more edge functionalities. Meanwhile, it is well proven that perfect 2D materials with covalent bonds are not permeable to many ions and gas molecules. Out-of-plane tortuosity, defined as the actual length to the point−point direct length, decreases from infinity in perfect 2D materials to a minimum of 1 through plane. By creating holes on 2D materials, better layer−layer stacking is also possible, leading to improved in-plane transport.

Related to material processing, H2D materials can dramatically improve composite manufacturing due to the fast removal of solvent or gas through holes. The major gap between the outstanding properties in individual 2D materials and their macroscopic counterparts is the poor stacking density. Dense structures lead to excellent layer−layer contact toward high thermal and electrical conductivity. While P2D materials are a perfect barrier for small molecules, H2D materials allow fast escape of gas molecules and solvent when the hole sizes are large enough. Such fast escape and transport of molecules (*e.g.*, water and air) is critical for fast manufacturing toward dense mesoporous structures.

In this work, we demonstrate that holey graphene, thermally treated graphene with through-thickness nanosized holes distributed in its basal plane (denoted as h-graphene hereafter), can be easily cold-pressed into dense and strong monoliths. In sharp contrast, pristine graphene, *i.e.*, untreated intact graphene, processed under the same conditions formed a weak and loose product that readily fell apart. Our mechanics modeling revealed a mechanistic understanding of the striking compressibility of h-graphene and the sharp contrast between h-graphene-based and pristine graphene-based cold-pressed products. Figure 2 presents digital photos of h-graphene powder and its monoliths in geometries of a disk, a bar, a sphere, and an arc made by uniaxial cold-pressing. The single-phase graphene monoliths with shiny lateral surfaces were

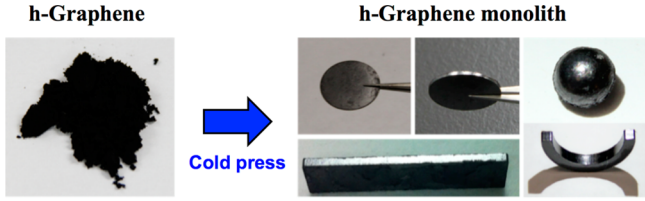

Figure 2. Digital photos of h-graphene and its monoliths with various geometries fabricated by cold pressing in a binder-free dry process. The diameters of the disks and sphere are 1.27 and 0.5 cm, respectively. The outer diameter of the arc is 2 cm with the wall thickness of 0.25 cm. The dimensions of the bar are 6 cm (length) × 0.6 cm (width) × 0.1 cm (thickness).

experimentally proven to be highly dense, mechanically robust, and electrically and thermally conductive, they were also shown to be machinable and exhibited excellent thermal dissipation characteristics. The dry process is free of any solvents and binders, thus overcomes all the disadvantages of wet processes, especially significant for the currently burgeoning industrial applications for graphene.

RESULTS AND DISCUSSION

The remarkable compressibility of h-graphene was demonstrated by compressing pristine graphene and h-graphene. h-Graphene was first synthesized by heating graphene directly in air under controlled conditions (*e.g.*, heated at 430 °C for 10 h as a typical example unless otherwise specified; see more details in Materials and Methods).[36,37] Detailed characterization data suggested that, during the synthesis under a moderate oxidation temperature (*e.g.*, 430 °C), the defective carbons on the pristine graphene sheets were preferentially oxidized and gasified (converting into CO and/or CO_2), leaving behind holes distributed on the graphene lateral surface.[37] More aggressive conditions such as a higher temperature or a longer duration could result in further gasification of the remaining graphitic carbon and thus enlarged holes. The scanning electron microscopy (SEM) image in Figure 3A shows a typical pristine graphene morphology with some wrinkles, and no holes were observed, while in Figure 3B many through-thickness holes with diameters of 10−20 nm distributed in the basal plane can be observed. Despite the presence of holes, these h-graphene sheets exhibited very similar layer numbers (~5−15 layers) and

DOI: 10.1021/acsnano.7b00227
ACS Nano XXXX, XXX, XXX−XXX

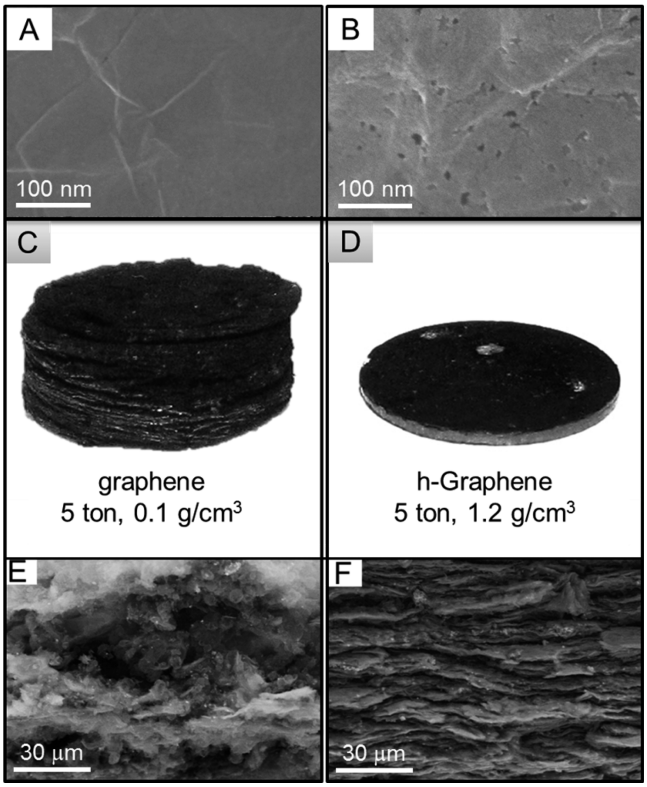

Figure 3. Remarkably different compressibility between pristine graphene and h-graphene (prepared at 430 °C/10 h) compressed pellets. (A, B) SEM images for pristine graphene (A) and h-graphene (B). (C, D) Digital photos of pressed pristine graphene (C) and h-graphene (D) pellets under identical conditions (sample mass, 60 mg; applied weight and duration, 5 ton for 10 min). The diameters of the disks are 1.27 cm. (E, F) Corresponding cross-section SEM images for pressed pristine graphene (C) and h-graphene (D) pellets.

lateral dimensions (~2−10 μm) compared to the pristine sheets.[36,37] The pristine graphene and h-graphene samples were then separately compressed in a pellet die under identical conditions including sample mass, applied weight, and duration. The pristine graphene formed loose pellets with visible gaps between layers and low apparent densities (*e.g.*, ~0.1 g/cm^3 in Figure 2C) and were easily broken during handling. In sharp contrast, h-graphene formed much thinner and denser pellets with high apparent density (*e.g.*, ~1.2 g/cm^3 in Figure 2D), more than 10 times higher than those of pristine graphene pellets. Moreover, these h-graphene-based pellets exhibited substantial robustness in handling. The same phenomenon was also observed when coaxial pressing h-graphene powder into other geometric monoliths (Figure 1 and Figure S1 in the Supporting Information). Unequivocally, it demonstrates the remarkable characteristics of h-graphene.

Figure 3E and F compare the morphology for the pressed pristine graphene and h-graphene pellets by cross-section SEM images. Clearly, the pristine graphene pellet consisted of randomly arranged flakes with many large voids in between, exhibiting a low packing density (Figure 3E). In sharp contrast, the h-graphene pellet consisted of tightly arranged flakes with much fewer and smaller voids, exhibiting a significantly higher packing density (Figure 3F). The reproducible SEM results accounted for the distinct difference of the apparent density of h-graphene pellets from pristine graphene pellets.

The fundamental mechanism accounting for the compressibility of h-graphene was revealed by atomistic simulations. It has been well-known that pristine intact graphene is not permeable to gas species.[38,39] As demonstrated below, the holes through the basal plane of h-graphene enabled high permeability of gas molecules during cold-pressing, a pivotal feature to enable any trapped gas to diffuse out of the stacked nanosheets. Figure 4A and B show the simulation models of

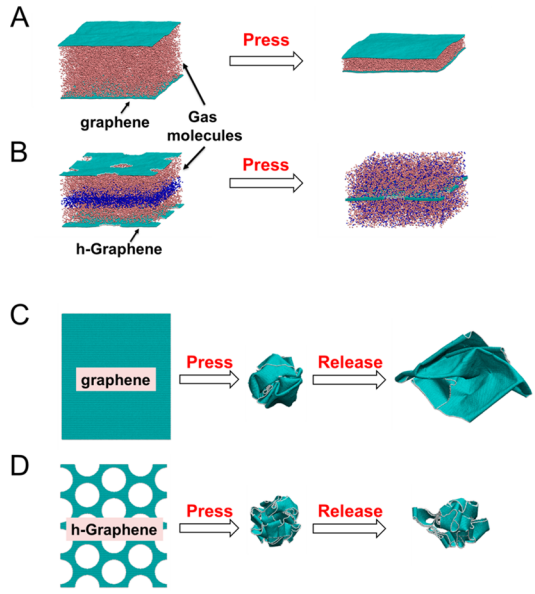

Figure 4. Atomistic simulations reveal a mechanistic understanding of the huge differences in compressibility of pristine graphene and h-graphene. (A, B) Demonstration of permeability of gas molecules through pristine graphene (A) and h-graphene (B). Gas molecules can diffuse more easily from h-graphene through its holes, leaving a more compact structure. (C, D) Demonstration of compressibility and rebounding of pristine graphene (C) and h-graphene (D) when external pressure is applied and then released, regardless of the trapped gas. After release, h-graphene maintains a highly compressed structure, while pristine graphene tends to rebound as far as possible.

nitrogen molecules (N_2) confined between two pristine graphene monolayers and two h-graphene monolayers, respectively. Periodical boundary conditions were used in the two in-plane directions of pristine graphene (or h-graphene) layers, so that the model effectively simulated gas molecules sandwiched in between two large neighboring graphene (pristine or holey graphene) layers, representative of the cold-pressing experiments. When a pressure is applied on the top and bottom of pristine graphene monolayers (Figure 4A), the initial block of gas molecules is squeezed into a thinner block, but the gas molecules still remain trapped in between the graphene bilayer. Upon the release of pressure, the squeezed gas molecules expand and separate the layers, leading to the loose and porous structure as shown in Figure 3C and E. By contrast, when a pressure is applied on h-graphene layers (Figure 4B), the initially trapped gas molecules can easily migrate and escape through the holes. By highlighting the gas molecules in two colors both nitrogen, the mixing of the gas molecules during their migration through the holes is clearly captured (Figure 4B and Movie S1 in the Supporting Information), demonstrating the dynamic and effective process of squeezing the gas molecules out of the h-graphene bilayer.

DOI: 10.1021/acsnano.7b00227
ACS Nano XXXX, XXX, XXX−XXX

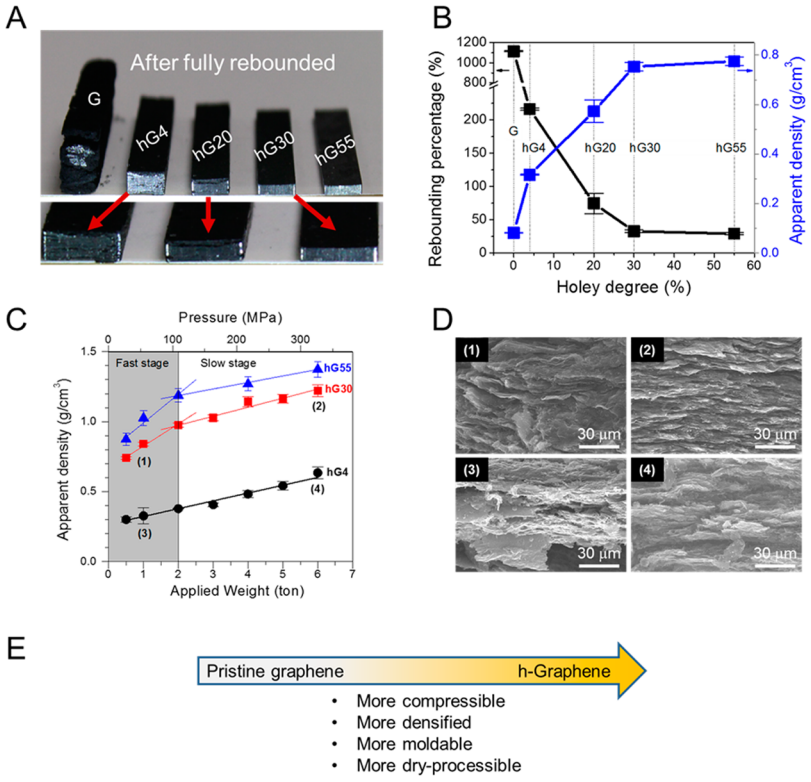

Figure 5. Effect of holey degree and applied pressure on h-graphene monolith compressibility and density. (A) Digital photo of pressed monolithic bars made from pristine graphene (G) and h-graphene (hG4, hG20, hG30, and hG55). (B) Plot of rebounding percentage and apparent densities of graphene monoliths as a function of holey degree. (C) Plot of the apparent density for hG4, hG30, and hG55 monoliths as a function of applied pressure. The shaded area refers to the fast stage of the hG30 monolith density evolution with applied pressure, and the rest is attributed to the slow stage. (D) Cross-section SEM images for corresponding samples labeled 1−4 in (C). (E) Schematic summary of the effects of holes on graphene dry-processability. The error bars in (B) and (C) were calculated from three separate measurements.

The above simulated situation can readily occur throughout the whole h-graphene monolithic sample during pressing so that initially trapped gas molecules can easily permeate through h-graphene flakes and be squeezed out from the resulting monoliths, leading to highly compact structures as shown in Figure 3D and F.

Our atomistic simulations further reveal another key mechanism that contributes to the remarkable compressibility of h-graphene when no significant gas in between layers can escape with compressing. The sample is subjected to compressive forces not only from the direct external loading but also from the spatial confinement, *i.e.*, the inner wall of the die. Although a uniaxial pressing was performed in the experiments here, in order to mimic an extreme condition of the spatial confinement by simulations, a suitable hydrostatic pressure is applied on both pristine graphene and h-graphene (with the same global geometrical dimensions) to deform them into pressed morphologies (middle illustration in Figure 4C and D). Upon stabilization, the applied hydrostatic pressure is released in the simulation. The compressed pristine graphene springs back substantially in volume (Figure 4C), while the compressed h-graphene maintains its structural morphology with only modest rebounding (Figure 4D). Such an apparent difference can be understood as follows. When h-graphene layers are compressed, the deformation of the layers is mainly accommodated by the folding and collapsing of h-graphene ribbons demarcated by the holes. By contrast, when pristine graphene layers are compressed, the deformation of the layers is mainly accommodated by wrinkling and folding the planar graphene layer, which can easily lead to long and sharp creases as well as asperities. Consequently, the resulting strain energy in the compressed pristine graphene is much higher than that in the compressed h-graphene. Furthermore, the much-increased length of hole edges can also allow for facile interaction sites, offering additional anchoring of the compressed structural morphology. As a result, upon releasing, compressed pristine graphene tends to expand as far as possible to relax the excess strain energy, while the compressed h-graphene rebounds just slightly (Movies S2 and S3 in the Supporting Information), an intrinsic feature contributing to the superior compressibility of h-graphene as observed in experiments. In our model, hydrogen terminating the graphene edges' chemical functionalization was introduced in order to prevent the bonding formation between the hole edges in h-graphene, where there are many dangling carbon bonds. Without hydrogen termination, under compression, the hole edges can easily bond to each other to minimize the number of dangling bonds. As a result, the "defected" h-graphene would be, in principle, more resistive to shape recovery than a pristine graphene because such carbon−carbon bonds formed along hole edges prevent the structure from recovering its original shape, while the pristine graphene would have much less of this effect. That being said, by introducing edge functionalization along hole edges in our model, the bond formation among hole edges was minimized and modeling results still showed that the h-graphene has much less shape recovery than pristine graphene. In other words, in real samples where dangling bonds (and oxygen-containing functional groups[37]) could exist along hole edges, such a difference

DOI: 10.1021/acsnano.7b00227
ACS Nano XXXX, XXX, XXX−XXX

between h-graphene and pristine graphene is even more significant, in agreement with the mechanistic understanding emerging from the modeling study. Both the mechanisms manifest that the holes in h-graphene play very important roles for the compressibility. It has been systematically studied previously[40] that graphene patterned with hole defects becomes significantly less rigid than pristine graphene. The larger the hole defects, the more compliant the holey graphene is. As a result, h-graphene would be easier to be stretched or compressed than pristine graphene.

To further investigate the influence of the hole size and distribution on graphene compressibility, four h-graphene samples were synthesized with different "holey degrees". For simplification, the holey degree of h-graphene was defined as the mass loss in percentage during the sample synthesis due to partial oxidation of pristine graphene. The samples were labeled hG4, hG20, hG30, and hG55, where the numbers indicate the percentage of mass loss (*i.e.*, "holey degree"). For example, hG30 means h-graphene sample with a holey degree of 30%. The higher the number, the higher the holey degree and the larger the average hole size and area in the h-graphene flakes (Figure S2 in the Supporting Information).

It is rational that less rebounding leads to higher compressibility. To observe and compare the compressibility, a rebounding test was designed. Equal amounts of pristine graphene and the above four h-graphene samples (120 mg each) were pressed to identical thicknesses (initial thickness, T_0) for 10 min respectively in a uniaxial die (Figure S3 in the Supporting Information). In the period of holding time, all the pressed monoliths were confined in the bar die to have the same volume of 30 mm (length) × 6 mm (width) × 0.67 mm (T_0) and density of 1.0 g/cm^3 and then released to allow complete rebounding. The final thickness (T_R) of the rebounded monoliths was subsequently measured. Figure 5A shows digital photos of the resultant monolithic bars. Clearly, the bars had diverse thicknesses, implying each had a different degree of rebounding. More quantitatively, the rebounding percentage was calculated from $(T_R - T_0)/T_0 \times 100\%$. Figure 5B exhibits the rebounding percentages with the sample holey degree. The rebounding percentage was dramatically reduced from 1130% for pristine graphene (denoted as G) to 220% for hG4 and then steady decreased to 75% for hG20 and 33% for hG30 (a remarkable 34-fold decrease), respectively. After that, the rebounding percentage approached a plateau (*e.g.*, 27% for hG55). This phenomenon of the holey degree-based rebounding can be explained by the percolation effect. With increasing holey degree, the increased pores and channels formed in h-graphene monoliths allow rapid and complete diffusion of the trapped air and thus less and less rebounding of the monoliths. When the holey degree reaches more than 30%, the pores and channels are sufficient for most trapped air to escape during pressing. A higher holey degree does not lead to more rapid or efficient diffusion, and thus a plateau of the rebounding degree is achieved. A holey degree of 30% appears to be the percolation threshold. These rebounding behaviors were reflected in the monolith appearance (Figure 5A). The monoliths of G, hG4, and hG20 with high rebounding showed obvious delamination, while the monoliths of hG30 and hG55 with low rebounding (or good compressibility) showed very well-compacted structure. The monolith density also shows a similar percolation effect with holey degree (Figure 5B). The density of h-graphene monoliths, and thus the compressibility of h-graphene powder, increased in conjunction with holey degree. Compared with hG30, hG55 has a much higher holey degree, but hG55 exhibits a similar density and compressibility, which is attributed to the 30% holey degree threshold. For the consideration of both the compressibility and synthesis yield (yield = 100% − holey degree), hG30 was selected as the optimum material for dense graphene monolith fabrication.

Figure 5C shows that the apparent density of the hG30 monoliths increased with the applied weight (pressure). It was observed that there are two apparent slopes associated with the density change. From 0.5 to 2 ton, the hG30 monolith density increased quickly with a slope of 0.16 (g/cm^3)/ton, while from 2 to 6 ton, it was only 0.056 (g/cm^3)/ton: a fast stage and a slow stage. This suggests a two-stage evolution of the graphene monoliths as a function of pressure. At the fast stage, the h-graphene monolith density increases rapidly due to the diffusion of trapped air. When most of the trapped air has diffused out of the monolith, subsequent diffusion becomes slower and needs significantly higher pressures to mainly squeeze graphene flakes and force the remaining trapped air out. The turning point of hG30 monolith density evolution with pressure occurs at about 2 ton (110 MPa). Due to similar compressibility to hG30, hG55 was expected to also exhibit a two-stage density evolution with the same turning point at 2 ton. This behavior is demonstrated in Figure 5C.

A sample with poor compressibility was also tested for the two-stage evolution. Since G monoliths were not sufficiently compressible, hG4 was employed to investigate this phenomenon. The results are shown in Figure 5C. In contrast, all the hG4 data points exhibited a linear fit with a slope of 0.058 (g/cm^3)/ton. Considering the poor compressibility of hG4, the linear relationship should be the fast stage in hG4 monolith density evolution with pressure. The turning point of hG4 monolith density could appear at a much higher pressure that is beyond the pressure limitation of the die and consequently was not observed in this work.

Figure 5D presents the typical cross-section SEM images for the monolithic samples marked in Figure 5C, *i.e.*, hG30 and hG4 at an applied weight of 1 ton and 6 ton, respectively. The packing density of hG30 appears significantly higher than that of hG4 either at 1 ton or 6 ton, in agreement with the monolith apparent densities (Figure 4C). The samples (hG30,1ton), (hG4,1ton), and (hG4,6ton) are located at their fast stages in terms of the two-stage pressing model (Figure 5C), implying the existence of remaining trapped air in the monoliths. The voids are easily found in the corresponding SEM images (Figure 5D (1), (3), (4)) for the three samples. In contrast, the sample (hG30,6ton) is located at its slow stage, implying that most trapped air has been expelled. It is evidenced by the very compact structure of hG30 flakes in Figure 5D (2). These typical morphologies of the pressed monoliths strongly support the two-stage pressing model. Figure 5E schematically summarizes the hole effects that enable graphene to be more compressible, densified, moldable, and dry-processable. Interestingly, these hG monoliths exhibited only a minor reduction in Brunauer−Emmett−Teller specific surface area (*e.g.*, ∼310 m^2/g for a hG30 disc pressed at 4 ton *vs* ∼370 m^2/g for as-produced hG powder) as measured by using a nitrogen desorption/adsorption technique (Quantachrome Nova 2200e surface area and pore size analyzer system with a 9 mm bulbless cell), suggesting that they might be useful for applications such as electrodes for energy storage.

The as-prepared hG30 monoliths exhibited outstanding mechanical durability compared to G monoliths, pressed

DOI: 10.1021/acsnano.7b00227
ACS Nano XXXX, XXX, XXX−XXX

carbon black, graphite flakes, and graphite powder (spherical graphite, 20 nm in diameter) monoliths made under the same conditions. Figure S4 in the Supporting Information shows the drop test results for these samples with geometries of disks and bars. All the samples were fractured when dropped from a height of 36 cm, while the hG30 maintained its integrity even after falling from a height of 110 cm (Movies S4–S6 in the Supporting Information). For quantitative study, tensile tests were performed for hG4, hG30, and hG55 monoliths processed under different pressures. In Figure 6A, the results of a specific

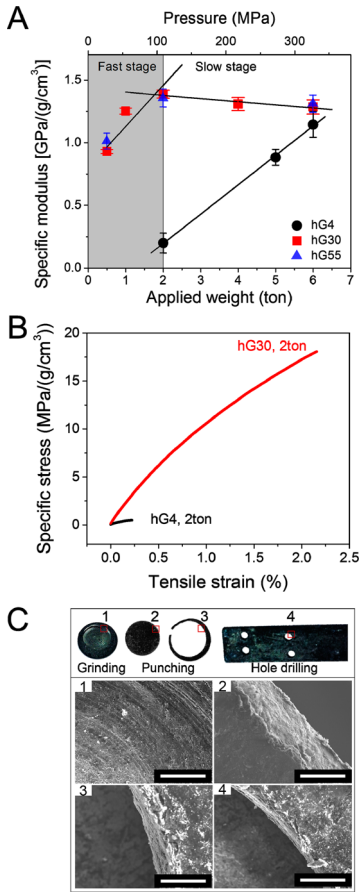

Figure 6. Mechanical properties and processability of the as-prepared h-graphene monoliths. (A) Specific modulus, (B) specific tensile strength, and (C) machining. The upper panels in (C) are digital photos of monolithic products of (hG30,2ton) obtained by mechanical grinding, punching, and hole drilling. The bottom panels are the SEM images for the corresponding square parts marked with numbers 1, 2, 3, and 4 in the upper photos. The shading area in (A) refers to the fast stage of the specific modulus evolution of the hG30 monolith with applied weight, and the rest is the slow stage. The error bars in (A) were calculated from three separate measurements. All the scale bars in (C) are 300 μm.

modulus (normalized modulus by apparent density) that reflects the intrinsic material property are shown. Similar to the density evolution, there also appears to be two stages for the specific modulus maximization of hG30 monoliths with applied pressure that occurred at about 2 ton (Figure 6A). For a pressure of less than 2 ton, the specific modulus increased rapidly, forming a steep slope, and for a pressure above 2 ton, the specific modulus nearly plateaued. This can be interpreted by the two-stage pressing model. During the first stage, the existence of trapped air restrains not only packing density but also the intermesh and cohesion force between the flakes in the monoliths. Therefore, with the expelling of trapped air, the specific modulus improves significantly. In the second stage when most of the trapped air is removed, the property was mainly controlled by graphene itself. The hG30 monolith showed almost a constant specific modulus at this stage, independent of applied pressure. Further, the corresponding data points of hG55 perfectly fell on the fitted lines of the hG30 specific modulus in Figure 6A, which is attributed to the similar compressibility and structure of hG55 and hG30. The hG4 monoliths exhibited the fast stage only for the specific modulus evolution in the pressure range studied. These results strongly supported the hypothesis of trapped-air-escaping-controlled first stage and graphene material restacking-controlled second stage for h-graphene monolith properties. The applied weight of 2 ton can be selected as the lowest pressure for fabrication of hG30 monoliths with high specific elastic modulus. Figure 6B shows the tensile stress–strain curves for hG30 and hG4 monoliths obtained at 2 ton. The hG30 monolith exhibited a specific tensile strength of 18.1 MPa/(g/cm^3) and a failure strain of 2.2%, while the hG4 monolith showed a specific tensile strength of 0.5 MPa/(g/cm^3) and a failure strain of 0.22%. In other words, the hG30 monolith is 36 times stronger and 300 times tougher (in terms of fracture energy, *i.e.*, the area below the stress–strain curve) than the hG4 monolith. According to the two-stage model, the monolith (hG30,2ton) is located in its second stage, while (hG4,2ton) is in its first stage, where the remaining trapped air in the monolith seriously limited its mechanical strength. It is important to note that the (hG30,6ton) monoliths had a tensile strength of 17 MPa, which is higher than that of conventional graphite (8 to 13 MPa).[41]

The pressed hG30 monoliths exhibited excellent mechanical properties and could be further mechanically processed with grinding, punching, and hole drilling. The upper digital photos in Figure 6C show the further processed hG30 monolithic products including a tray, a disk, a ring, and a piece of plate with drilling holes. The processing was facilely conducted using tools such as punchers, electric drills, or grinding wheels. The SEM images at the bottom in Figure 6C zoom in on the processed edges, showing the relatively smooth machining. It should be noted that the tray was made using a rough grinding wheel and left many circles on the surface. It is believed that more precise tools will produce more subtle bulky graphene products from the h-graphene monoliths.

The intimate contact of h-graphene flakes when compression molded is advantageous in maximizing bulk electrical and thermal conductivity. The results showed that for the same type of h-graphene monoliths the higher the apparent density, the higher the conductivity (both electrical and thermal). Thus, it is rational to infer that the h-graphene monolith conductivity would also exhibit a two-stage evolution with pressure. As shown in Figure 7A and B, both the electrical and thermal conductivities of hG30 monoliths exhibited the expected evolution with a turning point at 2 ton. The monolith conductivities increased more rapidly with pressure in the first stage (less than 2 ton) than in the second stage (above 2 ton). The results from hG55 nearly agreed with the fitted linear curves of hG30 (Figure 7A and B). In these data, the (hG30, 6ton) monolith presented a maximum electrical conductivity of 130 S/cm, and the (hG55,6ton) presented a maximum thermal conductivity of 20 W/mK. Although the thermal conductivity was significantly lower than that of monolayer graphene (details

DOI: 10.1021/acsnano.7b00227
ACS Nano XXXX, XXX, XXX–XXX

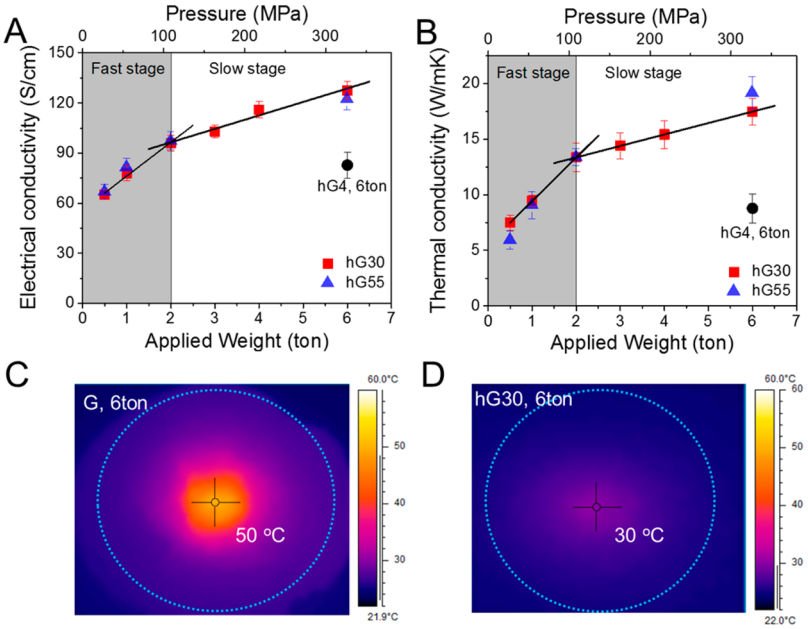

Figure 7. Electrical and thermal conductivities of h-graphene monoliths and thermal dissipation comparison for (G,6ton) and (hG30,6ton) monoliths. (A) Electrical and (B) thermal conductivities as functions of applied weight. (C, D) Steady-state temperature distribution on the surface of the pressed disks for (G,6ton) (C) and (hG30,6ton) (D) exposed to a hot spot created by a laser beam (1 mm in diameter) with controlled current at 7.5 A. The center numbers represent the highest temperatures in the corresponding images. The shaded area in (A) and (B) refers to the fast stage of the conduction evolution of the hG30 monolith with applied weight, and the rest is the slow stage. The error bars in (A) and (B) were calculated from three separate measurements. The diameters of the disks were 12.7 mm, and the ambient temperature is 23 °C for the thermal dissipation tests.

in the Supporting Information), it is much higher than that of most thermally conductive compounds (<10 W/mK)[42] and composites, *e.g.*, graphene/Al_2O_3 (8.28 W/mK).[43] Additionally, it is advantageous to use in severe situations such as moisture, corrosion, high temperature, and low thermal expansion rate, considering the graphene monoliths are single-phased lightweight carbon materials.

Due to poor mechanical properties, attempts to obtain the conductivity data for the G monoliths even when compression molded at 6 ton (G,6ton) were unsuccessful. The monolith (G,6ton) should have lower conductivities than the monolith (hG4,6ton), and the latter had lower conductivities than (hG30,6ton) (Figure 7A and B). To demonstrate the considerably improved thermal conductivity, an infrared thermal imaging method was applied on pressed disk (G,6ton) and (hG30,6ton). The thermal image shown in Figure 7C is the steady-state temperature distribution of the disk (G,6ton) surface exposed to a hot spot created by a laser beam. The highest temperature was 50 °C and notably distributed in the center area, showing a weak thermal dissipation ability of the monolith (G,6ton). In sharp contrast, Figure 7D presents a strong thermal dissipation performance of the monolith (hG30,6ton) under the same test condition. The heat from laser irradiation was dissipated promptly to the entire sample surface, and a faint high-temperature area was observed with a spike at 30 °C, which was slightly higher than the ambient temperature (23 °C). A higher thermal conductivity material allows localized heat to spread more easily; thus, for a given laser power a highly thermally conductive material exhibits a smaller temperature rise than one with low thermal conductivity. The monolith (hG30,6ton) significantly outperformed the monolith (G,6ton) in thermal conduction and dissipation.

CONCLUSION

This work demonstrated that single-phased dense graphene monoliths can be fabricated by compressing h-graphene at room temperature in an all-dry process. Both experimental and simulation results suggest the importance of holes and their contribution to the remarkable h-graphene compressibility by allowing trapped air to escape during pressing and preventing rebounding upon release of pressure. Further, a two-stage pressing model was proposed suggesting that during the initial compressing step the consolidation of the graphene monoliths is mainly dependent on the escape of the trapped air and then, in the second stage, the restacking of graphene flakes. The hypothesis explained the two slopes observed in the plots of monolith density, mechanical modulus, and both electrical and thermal conductivities as functions of applied pressure. The as-prepared h-graphene monoliths exhibited high density, excellent mechanical strength, and good electrical and thermal conductivity, in sharp contrast to compressed products of pristine intact graphene obtained under the same conditions. The h-graphene monoliths exhibited excellent machinability and outstanding thermal dissipation and thus have significant potential for various applications such as heat sinks and bipolar plates. With other properties such as retained high surface area and the ability to attain chemical functionalization at the hole edges of h-graphene sheets, these h-graphene monoliths can be a multifunctional platform toward applications such as energy storage, catalysis, sensing, and molecular separation, many of which are being pursued in our laboratories.[44,45]

In a broader context, this binder-free dry process presents a general approach for graphene and graphene-like 2D materials manufacture and development. The fact that holey 2D materials are intrinsically more manufacturable than their pristine counterparts without sacrificing their intrinsic proper-

DOI: 10.1021/acsnano.7b00227
ACS Nano XXXX, XXX, XXX−XXX

ties can be extended to many other 2D nanomaterials. This control will allow the manipulation of electrons, ions, photons, and phonons in and through the materials in a length scale ranging from individual 2D nanosheets to macroscopic structures. Future research can include the selective and optimized transport of ions or molecules through 2D stacked films for electrochemistry and sensor technologies, optimized mechanical properties that preserve the electronic properties of the materials for origami electronics.

MATERIALS AND METHODS

Synthesis of h-Graphene Powder. Briefly, the starting graphene, *i.e.*, pristine graphene (600 mg; Vor-X from Vorbeck Materials; grade: reduced 070; lot: BK-77x) was placed in an alumina crucible and heated in an open-ended tube furnace (MTI Corporation OTF-1200X-80-II) with a ramp rate of 10 °C/min and held isothermally at 430 °C for 1, 3, 10, and 20 h. h-Graphene products were directly obtained upon cooling the reaction and denoted as hG4, hG20, hG30, and hG55 according to the percent weight lost during the respective hold time.

Fabrication of h-Graphene Monoliths. Typically, 60 or 120 mg of h-graphene powder was measured and transferred to a stainless steel die. For facile pressing and demolding, two pieces of porous polypropylene (PP) membrane were used to sandwich the h-graphene powder in the die. The PP membrane, a plastic film, is often used as a separator in lithium-ion batteries. Due to the membrane's porous structure, the air squeezed from h-graphene during pressing can be expelled quickly through the membrane pores, and the PP membrane can be easily peeled off from the pressed h-graphene monolith, leaving a smooth surface. A hydraulic press (SPEX Sample Prep-Carver) was employed for the cold-press. Applied weight (W) was read from the pressure gauge directly, and corresponding pressure was calculated by $W \times g$/(sample top-view area) (g = 9.8 m/s^2). To reduce the error of press time, the press duration for all the samples shown in this article was 10 min. Then, by virtue of a micrometer and analytical balance the thickness and mass of the resultant h-graphene monoliths were recorded for density calculation. The pressed h-graphene monoliths with various shapes were made by using corresponding dies (Figure S5 in the Supporting Information). The same procedure was carried out for pristine graphene as control samples.

ASSOCIATED CONTENT

Supporting Information

The Supporting Information is available free of charge on the ACS Publications website at DOI: 10.1021/acsnano.7b00227.

Additional experimental details include photographic and SEM characterization, tensile tests of h-graphene monolith, thermal conductivity measurement of h-graphene monoliths, thermal dissipation measurement of h-graphene monoliths, simulation of molecular dynamics for h-graphene compressibility; additional figures include schematic illustrations of the rebounding test, results from drop tests, various custom-made dies used for monolithic architectures, and a schematic illustration for the thermal conductivity measurement (PDF)

Movie S1 (AVI)

Movie S2 (AVI)

Movie S3 (AVI)

Movie S4 (AVI)

Movie S5 (AVI)

Movie S6 (AVI)

AUTHOR INFORMATION

Corresponding Authors

*E-mail: yi.lin@nianet.org; yi.lin-1@nasa.gov.

*E-mail: binghu@umd.edu.

ORCID

Yi Lin: 0000-0002-1828-3518

Liangbing Hu: 0000-0002-9456-9315

Author Contributions

⊥X. Han and Z. Yang contributed equally to this work.

Notes

The authors declare no competing financial interest.

ACKNOWLEDGMENTS

L.H. and X.H. acknowledge NSF #1335979 and #1300361. We acknowledge the support of the Maryland NanoCenter and its AIMLab. Y.L. and J.W.C. acknowledge the support by the Internal Research and Development (IRAD) program from NASA Langley Research Center. T.L. and S.Z. acknowledge the support of NSF grants 1362256, 1069076, and 1129826. Z.Y. and B.Y. acknowledge the support of NSF grants 1232949 and 1336778.

REFERENCES

(1) Hernandez, Y.; Nicolosi, V.; Lotya, M.; Blighe, F. M.; Sun, Z.; De, S.; McGovern, I.; Holland, B.; Byrne, M.; Gun'Ko, Y. K. High-Yield Production of Graphene by Liquid-Phase Exfoliation of Graphite. *Nat. Nanotechnol.* **2008**, *3*, 563−568.

(2) Lotya, M.; Hernandez, Y.; King, P. J.; Smith, R. J.; Nicolosi, V.; Karlsson, L. S.; Blighe, F. M.; De, S.; Wang, Z.; McGovern, I. Liquid Phase Production of Graphene by Exfoliation of Graphite in Surfactant/Water Solutions. *J. Am. Chem. Soc.* **2009**, *131*, 3611−3620.

(3) Paton, K. R.; Varrla, E.; Backes, C.; Smith, R. J.; Khan, U.; O'Neill, A.; Boland, C.; Lotya, M.; Istrate, O. M.; King, P. Scalable Production of Large Quantities of Defect-Free Few-Layer Graphene by Shear Exfoliation in Liquids. *Nat. Mater.* **2014**, *13*, 624−630.

(4) Yi, M.; Shen, Z. A Review on Mechanical Exfoliation for the Scalable Production of Graphene. *J. Mater. Chem. A* **2015**, *3*, 11700−11715.

(5) Jeon, I.-Y.; Shin, Y.-R.; Sohn, G.-J.; Choi, H.-J.; Bae, S.-Y.; Mahmood, J.; Jung, S.-M.; Seo, J.-M.; Kim, M.-J.; Chang, D. W. Edge-Carboxylated Graphene Nanosheets *via* Ball Milling. *Proc. Natl. Acad. Sci. U. S. A.* **2012**, *109*, 5588−5593.

(6) Stankovich, S.; Dikin, D. A.; Piner, R. D.; Kohlhaas, K. A.; Kleinhammes, A.; Jia, Y.; Wu, Y.; Nguyen, S. T.; Ruoff, R. S. Synthesis of Graphene-Based Nanosheets *via* Chemical Reduction of Exfoliated Graphite Oxide. *Carbon* **2007**, *45*, 1558−1565.

(7) Li, D.; Mueller, M. B.; Gilje, S.; Kaner, R. B.; Wallace, G. G. Processable Aqueous Dispersions of Graphene Nanosheets. *Nat. Nanotechnol.* **2008**, *3*, 101−105.

(8) Abdelkader, A.; Cooper, A.; Dryfe, R.; Kinloch, I. How to Get between the Sheets: A Review of Recent Works on the Electrochemical Exfoliation of Graphene Materials from Bulk Graphite. *Nanoscale* **2015**, *7*, 6944−6956.

(9) Parvez, K.; Wu, Z.-S.; Li, R.; Liu, X.; Graf, R.; Feng, X.; Müllen, K. Exfoliation of Graphite into Graphene in Aqueous Solutions of Inorganic Salts. *J. Am. Chem. Soc.* **2014**, *136*, 6083−6091.

(10) Xu, Y.; Bai, H.; Lu, G.; Li, C.; Shi, G. Flexible Graphene Films *via* the Filtration of Water-Soluble Noncovalent Functionalized Graphene Sheets. *J. Am. Chem. Soc.* **2008**, *130*, 5856−5857.

(11) Tung, V. C.; Allen, M. J.; Yang, Y.; Kaner, R. B. High-Throughput Solution Processing of Large-Scale Graphene. *Nat. Nanotechnol.* **2009**, *4*, 25−29.

(12) Becerril, H. A.; Mao, J.; Liu, Z.; Stoltenberg, R. M.; Bao, Z.; Chen, Y. Evaluation of Solution-Processed Reduced Graphene Oxide Films as Transparent Conductors. *ACS Nano* **2008**, *2*, 463−470.

DOI: 10.1021/acsnano.7b00227
ACS Nano XXXX, XXX, XXX−XXX

(13) Jo, Y. M.; Yoon, S.; Lee, J.-H.; Park, S.-J.; Kim, S. R.; In, I. Submillimeter-Scale Graphene Patterning Through Ink-Jet Printing of Graphene Oxide Ink. *Chem. Lett.* **2011**, *40*, 54−55.
(14) Han, X.; Chen, Y.; Zhu, H.; Preston, C.; Wan, J.; Fang, Z.; Hu, L. Scalable, Printable, Surfactant-Free Graphene Ink Directly from Graphite. *Nanotechnology* **2013**, *24*, 205304.
(15) Jabari, E.; Toyserkani, E. Micro-Scale Aerosol-Jet Printing of Graphene Interconnects. *Carbon* **2015**, *91*, 321−329.
(16) O'Neill, A.; Khan, U.; Nirmalraj, P. N.; Boland, J.; Coleman, J. N. Graphene Dispersion and Exfoliation in Low Boiling Point Solvents. *J. Phys. Chem. C* **2011**, *115*, 5422−5428.
(17) Pham, V. H.; Cuong, T. V.; Hur, S. H.; Shin, E. W.; Kim, J. S.; Chung, J. S.; Kim, E. J. Fast and Simple Fabrication of a Large Transparent Chemically-Converted Graphene Film by Spray-Coating. *Carbon* **2010**, *48*, 1945−1951.
(18) Parviz, D.; Metzler, S. D.; Das, S.; Irin, F.; Green, M. J. Tailored Crumpling and Unfolding of Spray-Dried Pristine Graphene and Graphene Oxide Sheets. *Small* **2015**, *11*, 2661−2668.
(19) Wang, J.; Gao, X.; Wang, Y.; Gao, C. Novel Graphene Oxide Sponge Synthesized by Freeze-Drying Process for the Removal of 2, 4, 6-Trichlorophenol. *RSC Adv.* **2014**, *4*, 57476−57482.
(20) Zhang, R.; Cao, Y.; Li, P.; Zang, X.; Sun, P.; Wang, K.; Zhong, M.; Wei, J.; Wu, D.; Kang, F. Three-Dimensional Porous Graphene Sponges Assembled with the Combination of Surfactant and Freeze-Drying. *Nano Res.* **2014**, *7*, 1477−1487.
(21) Chavez-Valdez, A.; Shaffer, M.; Boccaccini, A. Applications of Graphene Electrophoretic Deposition. A Review. *J. Phys. Chem. B* **2012**, *117*, 1502−1515.
(22) Barzegar, F.; Bello, A.; Fabiane, M.; Khamlich, S.; Momodu, D.; Taghizadeh, F.; Dangbegnon, J.; Manyala, N. Preparation and Characterization of Poly (Vinyl Alcohol)/Graphene Nanofibers Synthesized by Electrospinning. *J. Phys. Chem. Solids* **2015**, *77*, 139−145.
(23) Yu, Y.-H.; Chan, C.-C.; Lai, Y.-C.; Lin, Y.-Y.; Huang, Y.-C.; Chi, W.-F.; Kuo, C.-W.; Lin, H.-M.; Chen, P.-C. Biocompatible Electrospinning Poly (Vinyl Alcohol) Nanofibres Embedded with Graphene-Based Derivatives with Enhanced Conductivity, Mechanical Strength and Thermal Stability. *RSC Adv.* **2014**, *4*, 56373−56384.
(24) Zhao, L.; Qiu, Y.; Yu, J.; Deng, X.; Dai, C.; Bai, X. Carbon Nanofibers with Radially Grown Graphene Sheets Derived from Electrospinning for Aqueous Supercapacitors with High Working Voltage and Energy Density. *Nanoscale* **2013**, *5*, 4902−4909.
(25) Eda, G.; Fanchini, G.; Chhowalla, M. Large-Area Ultrathin Films of Reduced Graphene Oxide as a Transparent and Flexible Electronic Material. *Nat. Nanotechnol.* **2008**, *3*, 270−274.
(26) Kong, B.-S.; Geng, J.; Jung, H.-T. Layer-By-Layer Assembly of Graphene and Gold Nanoparticles by Vacuum Filtration and Spontaneous Reduction of Gold Ions. *Chem. Commun.* **2009**, 2174−2176.
(27) Xu, Z.; Gao, H.; Guoxin, H. Solution-Based Synthesis and Characterization of a Silver Nanoparticle−Graphene Hybrid Film. *Carbon* **2011**, *49*, 4731−4738.
(28) Chabot, V.; Higgins, D.; Yu, A.; Xiao, X.; Chen, Z.; Zhang, J. A Review of Graphene and Graphene Oxide Sponge: Material Synthesis and Applications to Energy and the Environment. *Energy Environ. Sci.* **2014**, *7*, 1564−1596.
(29) Zhang, X.; Sui, Z.; Xu, B.; Yue, S.; Luo, Y.; Zhan, W.; Liu, B. Mechanically Strong and Highly Conductive Graphene Aerogel and Its Use as Electrodes for Electrochemical Power Sources. *J. Mater. Chem.* **2011**, *21*, 6494−6497.
(30) Hu, H.; Zhao, Z.; Wan, W.; Gogotsi, Y.; Qiu, J. Ultralight and Highly Compressible Graphene Aerogels. *Adv. Mater.* **2013**, *25*, 2219−2223.
(31) Tao, Y.; Xie, X.; Lv, W.; Tang, D.-M.; Kong, D.; Huang, Z.; Nishihara, H.; Ishii, T.; Li, B.; Golberg, D. Towards Ultrahigh Volumetric Capacitance: Graphene Derived Highly Dense but Porous Carbons for Supercapacitors. *Sci. Rep.* **2013**, *3*, 2975−2982.
(32) Yan, L.; Lin, M.; Zeng, C.; Chen, Z.; Zhang, S.; Zhao, X.; Wu, A.; Wang, Y.; Dai, L.; Qu, J. Electroactive and Biocompatible Hydroxyl-Functionalized Graphene by Ball Milling. *J. Mater. Chem.* **2012**, *22*, 8367−8371.
(33) Coleman, J. N.; Lotya, M.; O'Neill, A.; Bergin, S. D.; King, P. J.; Khan, U.; Young, K.; Gaucher, A.; De, S.; Smith, R. J. Two-Dimensional Nanosheets Produced by Liquid Exfoliation of Layered Materials. *Science* **2011**, *331*, 568−571.
(34) Xu, Y.; Lin, Z.; Zhong, X.; Huang, X.; Weiss, N. O.; Huang, Y.; Duan, X. Holey Graphene Frameworks for Highly Efficient Capacitive Energy Storage. *Nat. Commun.* **2014**, *5*, 4554−4561.
(35) Xu, Y.; Chen, C.-Y.; Zhao, Z.; Lin, Z.; Lee, C.; Xu, X.; Wang, C.; Huang, Y.; Shakir, M. I.; Duan, X. Solution Processable Holey Graphene Oxide and Its Derived Macrostructures for High-Performance Supercapacitors. *Nano Lett.* **2015**, *15*, 4605−4610.
(36) Han, X.; Funk, M. R.; Shen, F.; Chen, Y.-C.; Li, Y.; Campbell, C. J.; Dai, J.; Yang, X.; Kim, J.-W.; Liao, Y. Scalable Holey Graphene Synthesis and Dense Electrode Fabrication Toward High-Performance Ultracapacitors. *ACS Nano* **2014**, *8*, 8255−8265.
(37) Lin, Y.; Han, X.; Campbell, C. J.; Kim, J. W.; Zhao, B.; Luo, W.; Dai, J.; Hu, L.; Connell, J. W. Holey Graphene Nanomanufacturing: Structure, Composition, and Electrochemical Properties. *Adv. Funct. Mater.* **2015**, *25*, 2920−2927.
(38) Jiang, D.; Cooper, V. R.; Dai, S. Porous Graphene as the Ultimate Membrane for Gas Separation. *Nano Lett.* **2009**, *9*, 4019−4024.
(39) Berry, V. Impermeability of Graphene and Its Applications. *Carbon* **2013**, *62*, 1−10.
(40) Zhu, S.; Huang, Y.; Li, T. Extremely Compliant and Highly Stretchable Patterned Graphene. *Appl. Phys. Lett.* **2014**, *104*, 173103.
(41) Jackson, J.; Freed, M. The Effect of Specimen Geometry on the Tensile Strength of Graphite. *Carbon* **1965**, *3*, 257−259.
(42) Gwinn, J. P.; Webb, R. Performance and Testing of Thermal Interface Materials. *Microelectron. J.* **2003**, *34*, 215−222.
(43) Zhou, M.; Lin, T.; Huang, F.; Zhong, Y.; Wang, Z.; Tang, Y.; Bi, H.; Wan, D.; Lin, J. Highly Conductive Porous Graphene/Ceramic Composites for Heat Transfer and Thermal Energy Storage. *Adv. Funct. Mater.* **2013**, *23*, 2263−2269.
(44) Walsh, E. D.; Han, X.; Lacey, S. D.; Kim, J.-W.; Connell, J. W.; Hu, L.; Lin, Y. Dry-Processed, Binder-Free Holey Graphene Electrodes for Supercapacitors with Ultrahigh Areal Loadings. *ACS Appl. Mater. Interfaces* **2016**, *8*, 29478−29485.
(45) Lacey, S. D.; Walsh, E. D.; Hitz, E.; Dai, J.; Connell, J. W.; Hu, L.; Lin, Y. Highly Compressible, Binderless and Ultrathick Holey Graphene-Based Electrode Architectures. *Nano Energy* **2017**, *31*, 386−392.

DOI: 10.1021/acsnano.7b00227
ACS Nano XXXX, XXX, XXX−XXX